



香港天文台  
HONG KONG OBSERVATORY

Reprint 904

Atmospheric Phenomena Observed over the South China Sea by the  
Advanced Synthetic Aperture Radar Onboard the Envisat Satellite

W. Alpers<sup>1</sup>, W. Huang<sup>2</sup>,

P.W. Chan, W.K. Wong, C.M. Cheng, & A. Mouche<sup>3</sup>

Proceedings of the Dragon 2 Programme Mid Term Results

Symposium, Guilin, P.R.China, 17-21 May 2010,

ESA publication SP-684

<sup>1</sup> Centre for Marine and Atmospheric Sciences (ZMAW), Institute of Oceanography,  
University of Hamburg, Hamburg, Germany

<sup>2</sup> State Key Laboratory of Satellite Ocean Environment Dynamics, Second Institute of  
Oceanography, State Oceanic Administration, Hangzhou, China

<sup>3</sup> CLS, Radar Applications, Bat. le Ponant, Avenue La pérouse, Technopôle  
Brest-Iroise, 29280 Plouzane, France

# **ATMOSPHERIC PHENOMENA OBSERVED OVER THE SOUTH CHINA SEA BY THE ADVANCED SYNTHETIC APERTURE RADAR ONBOARD THE ENVISAT SATELLITE**

**Werner Alpers**

*Centre for Marine and Atmospheric Sciences (ZMAW), Institute of Oceanography, University of Hamburg,  
Bundesstrasse 53, 20146 Hamburg, Germany, Email: [werner.alpers@zmaw.de](mailto:werner.alpers@zmaw.de)*

**Weigen Huang**

*State Key Laboratory of Satellite Ocean Environment Dynamics, Second Institute of Oceanography,  
State Oceanic Administration*

*No.36 Baochubei Road, Hangzhou, China, ZIP: 310012, Email: [wghuang@mail.hz.zj.cn](mailto:wghuang@mail.hz.zj.cn)*

**Pak Wai Chan, Wai Kin Wong , Cho Ming Cheng**

*Hong Kong Observatory, 134A Nathan Road, Hong Kong, China*

*Emails: [pwchan@hko.gov.hk](mailto:pwchan@hko.gov.hk), [wkwong@hko.gov.hk](mailto:wkwong@hko.gov.hk), [cmcheng@hko.gov.hk](mailto:cmcheng@hko.gov.hk)*

**Alexis Mouche**

*CLS, Radar Applications, Bat. le Ponant, Avenue La pérouse, Technopôle Brest-Iroise,  
29280 Plouzane, France, Email: [amouche@cls.fr](mailto:amouche@cls.fr)*

## **ABSTRACT**

Atmospheric phenomena often leave fingerprints on the sea surface, which are detectable by synthetic aperture radar (SAR). Here we present some representative examples of SAR images acquired by the Advanced Synthetic Aperture Radar (ASAR) onboard the Envisat satellite over the South China Sea (SCS) which show radar signatures of atmospheric gravity waves (AGWs) and of coastal wind fields. On SAR images of the SCS also often radar signatures of oceanic internal waves (OIWs) are visible which have similar spatial scales as the ones originating from AGWs. Therefore we first present criteria how to distinguish between them by analyzing the structure of the radar signatures. Then we present two examples of ASAR images which show radar signatures of AGWs over the SCS. Furthermore, we present a SAR image showing radar signatures of a

northerly Winter Monsoon surge event over the coastal area south of Hong Kong and compare it with a cloud image and a weather radar image. From the ASAR image we retrieve the near-surface wind field and compare it with the wind field simulated by the AIR model of the Hong Kong Observatory. The comparison shows that the AIR model can simulate quite well the wind speed as well as the position and shape of the frontal line measured by ASAR.

## **1. INTRODUCTION**

Synthetic aperture radar (SAR) images acquired over the ocean often show radar signatures of oceanic phenomena, like oceanic internal waves (OIWs), oceanic fronts, underwater sand banks or oil slicks, but also radar signatures of atmospheric phenomena, like atmospheric gravity waves (AGWs), atmospheric fronts,

cyclones or coastal wind fields. Often the radar signatures of oceanic and atmospheric phenomena look quite similar and it is not always easy to decide whether they originate from oceanic or atmospheric phenomena. This applies in particular to wave-like patterns which can be radar signatures of AGWs or OIW. In Section 2 we present criteria how to distinguish between these two types of waves and in Section 3 we present two examples of ASAR images acquired over the South China Sea (SCS) showing typical radar signatures of AGWs. In Section 4 we present a SAR image acquired by the Advanced Synthetic Aperture Radar (ASAR) onboard the Envisat satellite over the South China Sea (SCS) off the coast of Hong Kong on which radar signatures of a coastal wind field are visible which are associated with a northerly Winter Monsoon surge event (cold air outbreak).

We compare this ASAR image with a quasi-simultaneously acquired cloud image and a weather radar image from the Hong Kong Observatory. From this ASAR image the near-surface wind field is derived and compared with the wind field predicted by the new numerical weather prediction model operated by the Hong Kong Observatory, called AIR. The high resolution ASAR image reveals fine-scale details of the coastal wind field, including rain cells and AGWs propagating along the frontal line.

## 2. DISCRIMINATION BETWEEN ATMOSPHERIC GRAVITY WAVES AND OCEANIC INTERNAL WAVES

AGWs and OIW are ubiquitous phenomena in the atmosphere and in the ocean, respectively. But most often they have small amplitudes which makes it difficult to identify them in data records. However, exceptions are large amplitude nonlinear OIW and AGWs which appear in wave groups and which are

often described in terms of solitary wave (soliton) theory.

Both types of waves become visible on SAR images of the sea surface because they modify the sea surface roughness and thus the backscattered radar power or the normalized radar cross section (NRCS). In the case of AGWs, the variation in surface roughness is caused by variation in wind speed at the sea surface (or more precisely: of the surface stress) and in the case of OIW by the variation of the surface current.

Often the fingerprints of AGWs and OIW visible on SAR images have the same spatial scales and it is not always easy to determine whether the wave patterns result from AGWs or OIW. In Fig. 1 an ASAR image is depicted which shows at the same time radar signatures of both type of waves:

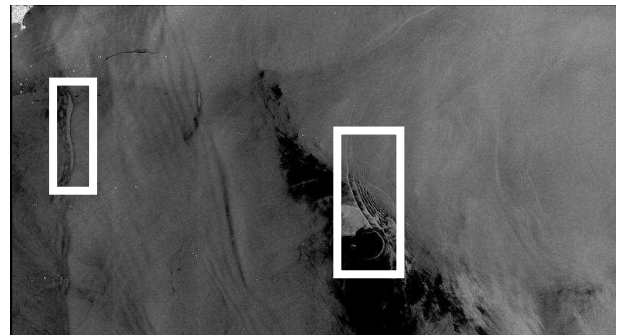


*Figure 1. Envisat ASAR WSM image acquired over the South China Sea around the Dongsha coral reef on 11 January 2008 at 0210 UTC showing radar signatures of atmospheric gravity waves and of oceanic internal waves. Imaged area: 400 km x180 km. © ESA*

(1) in the left box radar signatures of a solitary AGW and (2) in the right box of a nonlinear OIW packet. This ASAR image was acquired on 11 January 2008 at 0210 UTC in the Wide Swath Mode (WSM) over the SCS near the Dongsha coral reef. A zoom of both areas marked by boxes on the ASAR image is depicted in Fig. 2. It can clearly be seen that the structures of the radar signatures of both types of waves are quite different.

How radar signatures of AGWs are formed is shown schematically in Fig. 3. They result from the variation of the wind speed at the sea surface. This plot shows that the direction of the airflow is alternating at the sea surface. If the ambient wind is directed anti-parallel to the wave propagation direction (as it is most often the case), then the wind speed at the sea surface is reduced under the wave crests and enhanced under the wave troughs yielding an alternating roughness pattern on the sea surface and thus an alternating image intensity pattern on the SAR image. Under the wave crests the image intensity is reduced relative to the background and under the wave troughs it is enhanced.

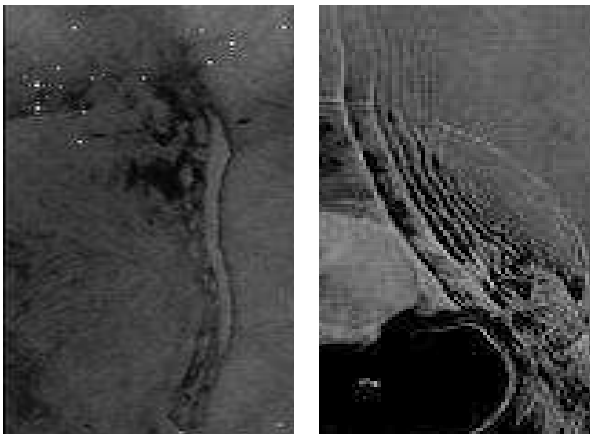


Figure 2. Zoom of the boxes inserted in the ASAR image of 11 January 2008 at 0210 UTC depicted in Fig. 1. It shows in the right box the Dongsha coral reef (visible as a half circle) and radar signatures of an OIW packet and in the left box radar signatures of a solitary AGW.

Since nonlinear AGWs are usually waves of elevation, the bright bands are much broader than the dark bands. Thus a nonlinear AGW packet shows up on a SAR image as a weak narrow dark band in front followed by a broad bright band, which is then followed again by a weak narrow dark band. This feature is repeated, but with reduced modulation strength, for the other solitary waves in the wave packet which have smaller

amplitudes. If the moisture content of the air is such that it allows the formation of clouds, then the clouds are positioned over the wave crests.

How radar signatures of OIW are formed is shown schematically in Fig. 4. They result from the variation of the surface current as described in [1]. Nonlinear OIW packets usually consist of solitary waves of depression. In Fig. 4, line (a) shows the shape of the pycnocline (boundary separating two water layers of different densities) in a 2-layer model, line (b) the variation of the short-scale sea surface roughness, and line (c) the variation of the NRCS or

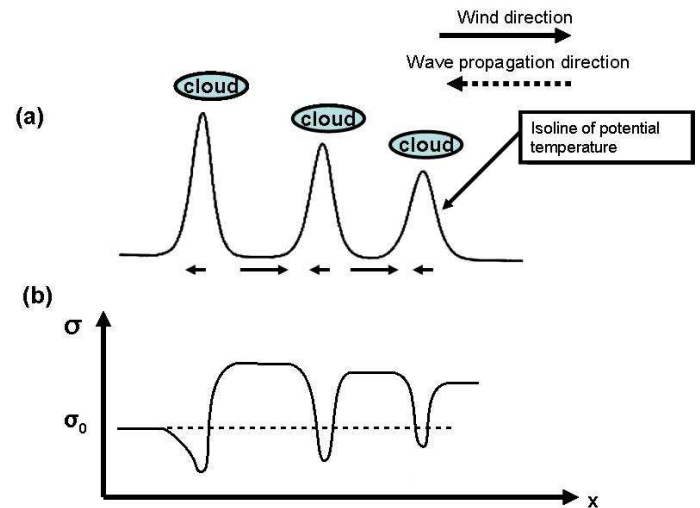


Figure 3. Schematic diagram illustrating the generation of the radar signature of a strongly nonlinear atmospheric wave packet consisting of three solitons of elevation: (a) Shape of an isoline of potential temperature. The arrows below the isoline denote the direction and the magnitude of the surface wind associated with the waves. The wind direction is defined here as the direction into which the wind is blowing. (b) Variation of the NRCS (or equivalently: of the SAR image intensity) caused by the solitary waves.  $\sigma_0$  denotes the background NRCS. Clouds are located over the low NRCS areas.

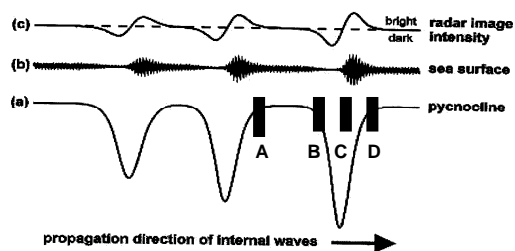


Figure 4. Schematic diagram illustrating the generation of the radar signature of a nonlinear oceanic internal wave packet consisting of three solitons of depression: (a) shape of the pycnocline in a 2-layer model, (b) variation of the short scale sea surface roughness, and (c) variation of the SAR image intensity (image brightness).

radar image intensity (image brightness) as a function of distance. The distances B-C and C-D give the widths of the bands with decreased and increased image brightness, respectively, and A-B the width of the band with background image brightness. Thus an OIW packet consisting of solitary waves of depression shows up on SAR images as a bright band in front followed by a narrow dark band. Then a much wider band of average (background) image brightness follows. This feature is repeated, but with reduced modulation strength, for the following waves in the wave packet.

Typical examples of radar signatures of nonlinear AGWs and OIWs are shown in Fig. 5. Radar signatures of nonlinear AGWs look smoother than the ones of nonlinear OIWs, which look more “crisp”. However, when the AGWs or OIWs are quasi-linear, then it is often not easy to decide from the structure of the radar signature alone whether the wave pattern originates from AGWs or OIWs. In these cases one has to recourse to other criteria [2]. For example, if the wave pattern is located on the downwind side of a coastal mountain or a mountainous island (see Fig. 6) or in a sea area where

the ocean is not stratified, then it must be of atmospheric origin.

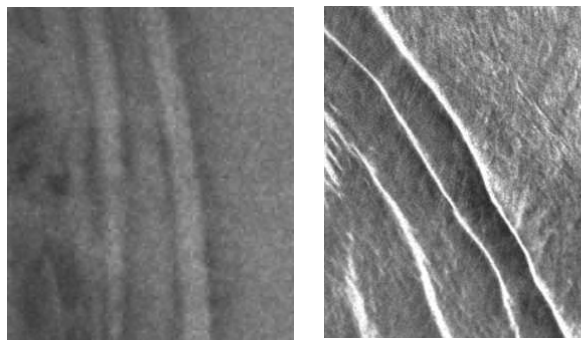


Figure 5. Typical examples of SAR images showing radar signatures of nonlinear atmospheric gravity waves (left) and nonlinear oceanic internal waves (right). The radar signature of a solitary atmospheric gravity wave consists of a wide bright band bordered by two narrow dark bands and the radar signature of a solitary oceanic internal wave consists of a bright band in front followed by a narrow dark band.

### 3. ATMOSPHERIC GRAVITY WAVES OVER THE SOUTH CHINA SEA

#### 3.1 Lee waves off the southwest coast of Taiwan

In Fig. 6 an ASAR image is depicted which was acquired in the Alternating Polarization (AP) mode over the sea area southwest of Taiwan on 21 Nov 2005 at 1402 UTC. It shows radar signatures of trapped AGWs in the lee of a mountain range in southern Taiwan [3]. Such AGWs are also called lee waves. They extend over a distance of more than 100 km and have a wavelength of about 5 km. A strong northeasterly wind of about  $20 \text{ ms}^{-1}$  was blowing over Taiwan and the adjacent seas as measured by QuikSCAT on 21 November 2005 at 1030 UTC (not shown here), see

[http://www.remss.com/qscat/qscat\\_browse.html](http://www.remss.com/qscat/qscat_browse.html).

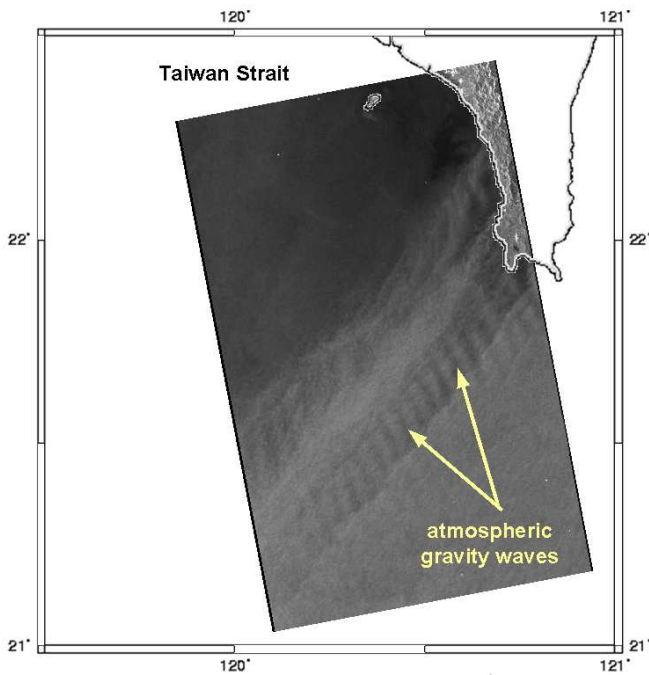


Figure 6. Envisat ASAR AP image acquired on 21 Nov 2005 at 1402 UTC (swath width: 100 km) over the Strait of Taiwan. Radar signatures of a 100 km long atmospheric gravity wave train are discernible in the wind shadow of a mountain range in southern Taiwan © ESA.

At the southern tip of Taiwan the airflow from the northeast is blocked by the mountain range forming a wind shadow southwest of Taiwan. In Fig. 7 the near-surface wind field is depicted which was retrieved from this ASAR image by using the CMOD 4 model [4] and by inferring the wind direction from the linear features visible on the ASAR image [5]. It reveals that in the very southern tip of Taiwan the airflow passed over a gap in the mountain range resulting in enhanced gap wind. Farther to the south, the wind blew around the southern tip of Taiwan unimpeded by mountains.

Thus a narrow wind-shadowed area was formed which was bordered on the northwest side by the gap wind and on the southeast side by the synoptic-scale wind. Thus this low wind speed area was bordered in the horizontal direction by two strong wind shear planes.

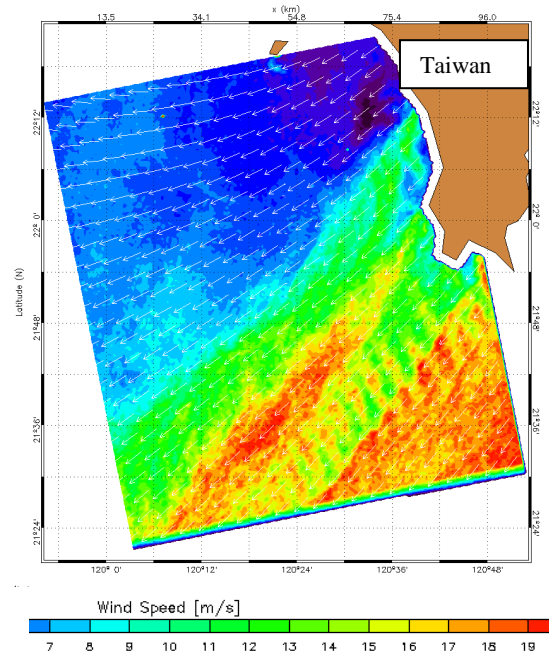


Figure 7. Near-surface wind field derived from the ASAR image depicted in Fig. 8 using the CMOD4 wind scatterometer model and the wind direction from the linear features visible on the ASAR image. Spatial resolution of the wind field is 500 m.

These horizontal wind shear boundaries formed the horizontal walls for the wave duct or wave guide. In the vertical direction, the lower boundary of the wave duct was the water surface and the upper boundary was the strong temperature inversion layer located at a height of about 1500 m as evidenced by radiosonde data acquired at Xiamen on 21 November 2005 at 1200 UTC. Thus, during this event, a wave duct with strong horizontal and vertical boundaries was present through which the AGWs could propagate over large horizontal distances with little attenuation.

The wind field map shows that the AGW caused a variation of the near-surface wind speed ranging from 12 to 18  $\text{m s}^{-1}$ .

### 3.2 Upstream atmospheric gravity waves off the east coast of Hainan

Fig. 8 shows an ASAR image which was acquired in the Image Mode (IM) on 13 March 2006 at 0236 UTC over the sea area east of Hainan. It shows radar signatures of upstream AGWs [6] off the southeast and northeast coasts of Hainan. Also here strong horizontal wind shear provided the lateral boundaries for the wave duct. Evidence that the wave patterns visible on this ASAR image are indeed radar signatures of AGWs is provided

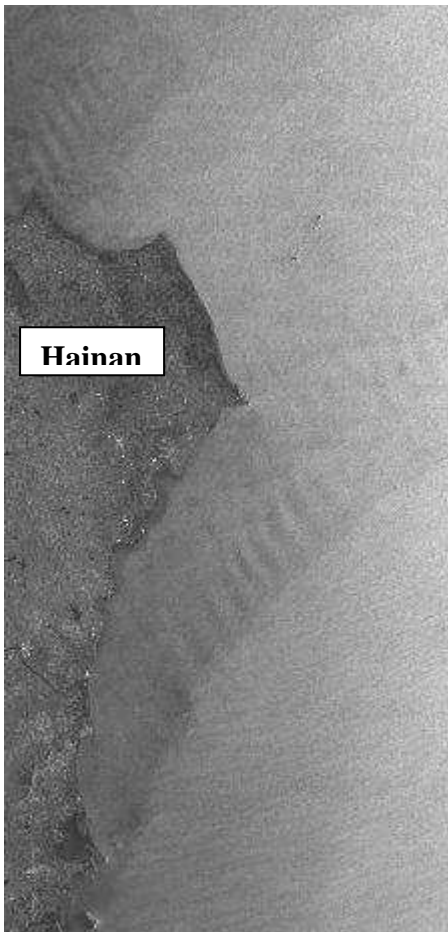


Figure 8. Envisat ASAR image acquired on 13 March 2006 at 0236 UTC in the Image Mode (IM) (swath width: 100 km) over the South China Sea near Hainan. Radar signatures of upstream AGWs trains are discernible north east and south east of Hainan. © ESA

by a cloud image acquired by the MODIS sensor onboard the Terra satellite on 13 March 2006 at 0531 UTC (not reproduced here) which shows wave patterns in the cloud distribution in the same location as the ASAR image. The wavelength of the AGWs is about 6 km.

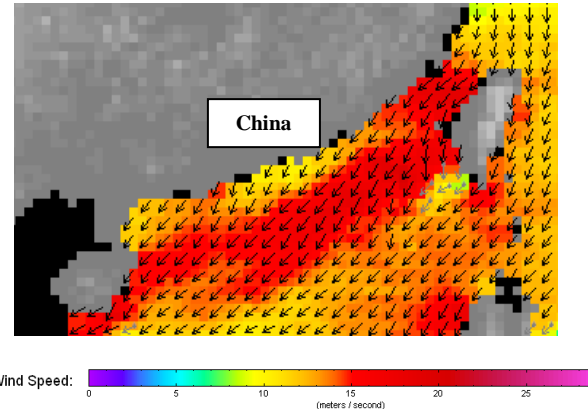


Figure 9. Wind field retrieved from Quikscat data acquired on 13 March 2006 at 1030 UTC. It shows a northeasterly wind of about  $20 \text{ ms}^{-1}$  blowing from the Strait of Taiwan against the east coast of Hainan.

The near-surface wind field retrieved from QuikSCAT data acquired on 12 March 2006 at 2142 UTC (4 hours and 54 minutes before the SAR data acquisition) is depicted in Fig. 9. It shows that a northeasterly wind of about  $20 \text{ ms}^{-1}$  was blowing against the east coast of the Chinese island of Hainan. Also the weather map of 13 March 2006 at 00 UTC shows northeasterly winds behind a trough of low pressure over the northern part of the South China Sea

## 4. COASTAL WIND FIELDS

Coastal wind fields at the northern coast of the SCS have often been observed on Envisat ASAR images, see, e.g., [7]. Here we present an ASAR image showing radar signatures of a northerly Winter Monsoon surge event over the SCS south of Hong Kong and compare it with quasi-simultaneously acquired other satellite and weather radar data as well as with model data.

#### 4.1 Observational data of a northerly Winter Monsoon surge event

In Fig. 10 an ASAR image is depicted which was acquired in the Wide Swath Mode (WSM) at VV polarization on 15 December 2009 at 1430 UTC over the northern coast of the SCS near Hong Kong (HK). This ASAR image was acquired during a cold air outbreak or a northerly Winter Monsoon surge event associated with the passage of a cold front, which carried cold air from a high pressure region over

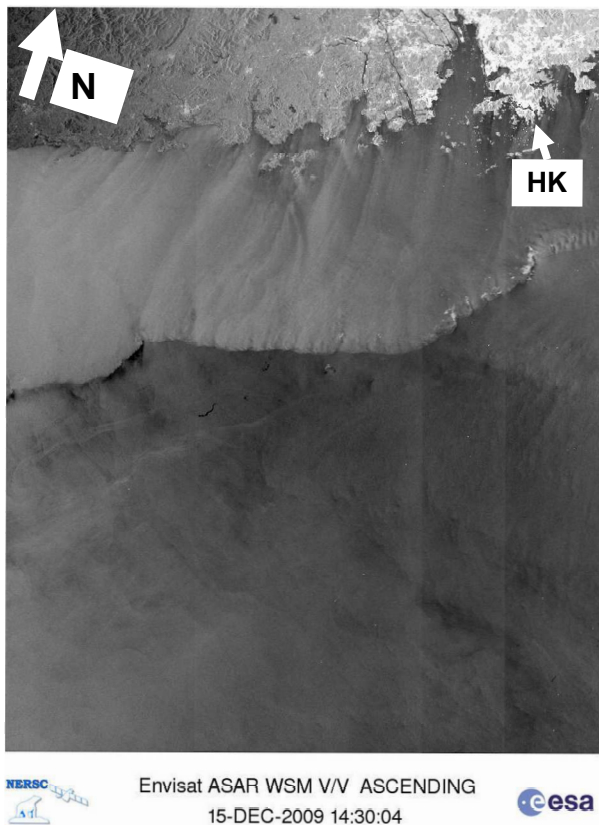


Figure 10. Envisat ASAR WSM image (VV polarization) acquired on 15 December 2009 at 1430 UTC over the north coast of the South China Sea near Hong Kong (HK). The imaged area is 400 km x 660 km. © ESA, Visible are wind jets caused by airflow through valleys.

Mongolia-Northern China to the SCS.

Fig. 11 shows a zoom on the sea area south of Hong Kong on which radar signatures of rain cells embedded

in the atmospheric front and of AGWs propagating along the front are visible.

While the radar signatures of the rain cells result here from radar backscattering at rain drops in the atmosphere (volume scattering), the radar signatures of AGWs result from radar backscattering at the sea surface (surface scattering) [8], [9]. Evidence that the bright spots located at the frontal line are indeed radar signatures of rain cells is provided by the simultaneously acquired weather radar image (at 1430 UTC) depicted in Fig. 12. It shows a map of the radar reflectivity converted into rainfall rate. Note that the

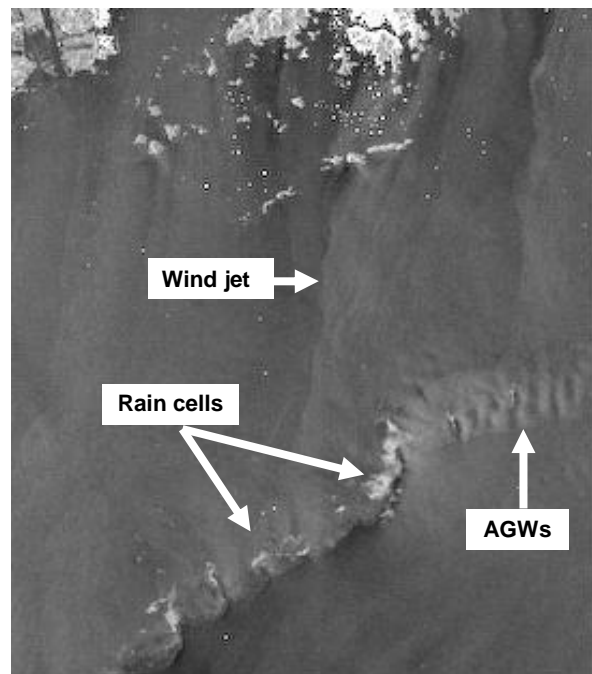


Figure 11. Zoom of the ASAR image depicted in Fig. 10 on the sea area south of Hong Kong showing radar signatures of rain cells embedded in the atmospheric front and radar signatures of atmospheric gravity waves (AGWs) propagating along the front.

bright spots on the ASAR image, which denote high radar reflectivity, are located at the same position as on the ASAR image (Fig. 11).

The AGW train was very likely generated by the downdraft associated with a rain cell, probably with the large rain cell located furthest east. It is well known that strong rain events associated with thunderstorms can generate AGWs (see, e.g., [10], [11]). Peculiar features visible in the AGW pattern are the two small bright spots which are located in the dark sections of the wave pattern. Here the wave crests are located, where warm air is uplifted from the sea surface. At these locations condensation can take place generating clouds and thus we suppose that the bright spots are radar signatures of small rain cells induced by the AGW. Such bright spots in the dark sections of AGW patterns have been observed occasionally also on other SAR images.

In Fig. 13 the near-surface wind field is depicted which was retrieved from this ASAR image by using the CMOD 4 model [4] and by inferring the wind direction from linear features visible on the ASAR image [5]. This wind field shows that near the coast a northerly

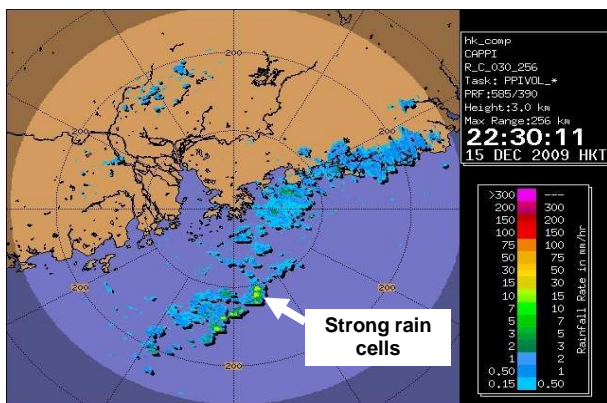


Figure 12. Reflectivity image converted into rain rate acquired by the Hong Kong weather radar on 15 December 2009 at 1430 UTC (2230 Hong Kong Time) showing the distribution of rain cells around Hong Kong. In particular, the strong rain cells embedded in the atmospheric front visible on the ASAR image depicted in Fig. 11 are also visible on this image.

wind with a speed between 5 and 15  $\text{ms}^{-1}$  was blowing from a northerly direction. It formed a sharp boundary with the easterly ambient wind field. The off-shore distance of the frontal line varied between 110 and 155 km. Embedded in the coastal wind field are wind jets which were generated by airflow funneled through coastal valleys and which have speeds of up to 15  $\text{ms}^{-1}$ .

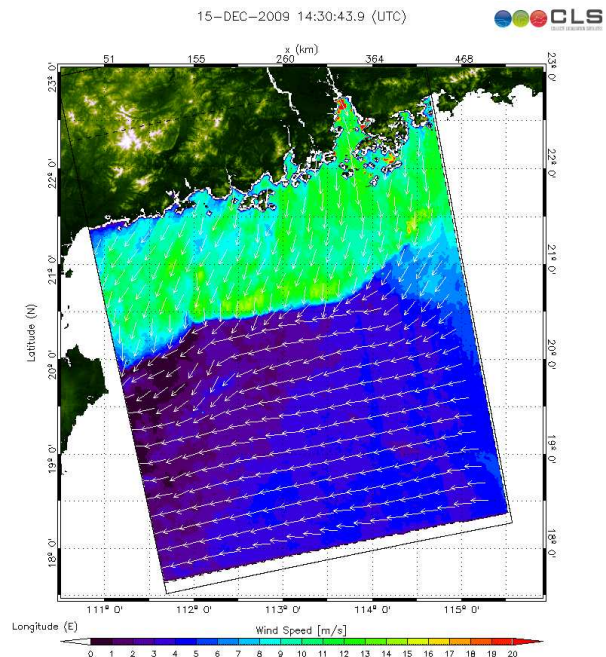


Figure 13. Near-surface wind field derived from the ASAR image depicted in Fig. 10 using the CMOD4 wind scatterometer model and the wind direction from the linear features visible on the ASAR image. Spatial resolution of the wind field is 500 m.

Noteworthy are the black regions on the south side of the front visible in the western section of the ASAR image (Fig. 10). We interpret them as radar signatures of oil slicks which accumulate in regions of surface flow convergence. This surface flow convergence is caused by two opposing wind drifts meeting at the frontal line.

After the passage of the cold front, the temperature at the Hong Kong Observatory headquarters dropped from

21 degrees C to a minimum of 13 degrees. The water temperature was 19 degrees C. When the cold air reached the coastline and advanced over the warm sea, a large amount of heat and water vapor was supplied to the air. This destabilized the lower troposphere creating a thick convective layer and a strong moisture flux upward leading to the formation of stratocumulus. The tops of these clouds have a lower temperature than the water surface. Thus the boundary between in the cloud-covered coastal region and the cloud-free region further south can be delineated on satellite images acquired in the thermal infrared band. In Fig. 14 a MODIS Thermal Composite image is depicted which was acquired on

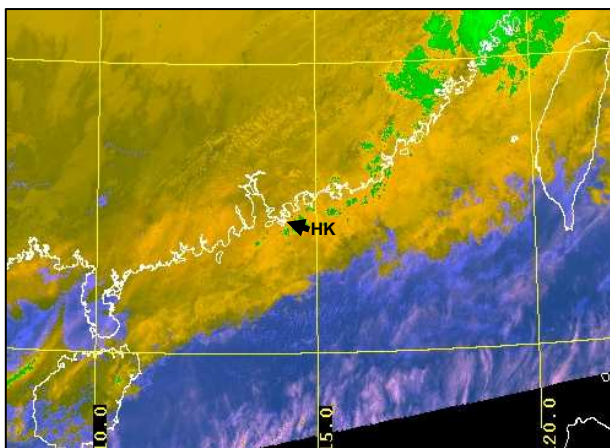


Figure 14. MODIS Thermal Composite image acquired on 15 December 2009 at 1435 UTC over the South China Sea and China showing cloud cover via temperature distribution. The yellow and green colors denote low temperatures associated with clouds. © NASA GSFC

15 December at 1435 UTC, i.e., only 5 minutes after the ASAR data acquisition. The yellow colors denote low temperature (clouds) and the blue colors warm temperature (water). Note that the position of the edge of the clouds correlates well with the position of the frontal line visible on the ASAR image depicted in Fig. 10 and also with the position of rain band visible on the weather radar image depicted in Fig. 12.

#### 4.2 Comparison with model data

The high-resolution wind fields retrieved from ASAR images can be used to validate numerical meso-scale atmospheric models. We have compared the wind field (Fig. 13) retrieved from the ASAR image depicted in Fig. 10 with the wind field predicted by the numerical weather prediction model operated by the Hong Kong Observatory, called Atmospheric Integrated Rapid-cycle (AIR) forecast system [12]. It provides rapidly updated analysis and numerical predictions from 1-12 hours to 3 days ahead. Figure 15 shows the forecast wind field calculated at 1500 UTC for the lowest model height and

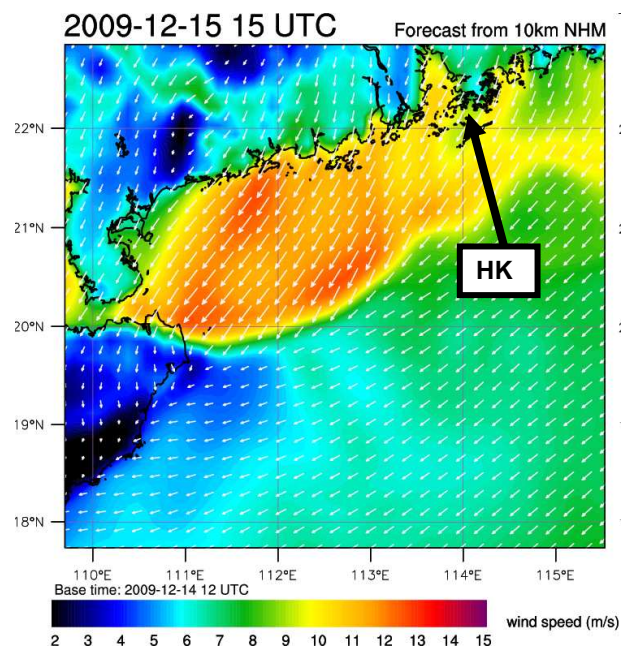


Figure 15. Near-surface wind field forecasted by the AIR model with a horizontal resolution of 10 km.

with a horizontal resolution of 10 km. (Since the model outputs are available only at full hours, a comparison with model data at 1530 UTC was not possible). The comparison of the simulated wind field (Fig. 15) with the one retrieved from the ASAR image (Fig. 13) shows that both wind fields agree quite well. This agreement applies to wind speed as well as to the position and shape of the frontal line.

## 5. CONCLUSIONS

SAR images acquired over the ocean yield unique information on the fine-scale structure of coastal wind fields and atmospheric gravity waves in the lower troposphere that cannot be obtained by other instruments. In particular, near-surface wind fields associated with these atmospheric phenomena can be retrieved from these SAR images with a resolution of few hundred meters. The SAR images constitute an excellent means to test and validate meso-scale atmospheric models.

## ACKNOWLEDGEMENT

We thank ESA for providing the ASAR images free of charge within the Dragon 2 project 5316.

## 6. REFERENCES

1. Alpers, W. (1985), Theory of radar imaging of internal waves, *Nature*, **314**, 245-247.
2. Alpers, W. & Huang, W. (2010), On the discrimination of radar signatures of atmospheric gravity waves and oceanic internal waves on synthetic aperture radar images of the sea surface, *IEEE Trans. Geosci. Rem. Sens.*, accepted, 2010.
3. Cheng, C.M. & Alpers, W. (2010), Investigation of trapped atmospheric gravity waves over the South China Sea using Envisat synthetic aperture radar images, *Int. J. Remote Sensing*, in press.
4. Stoffelen A. & Anderson, D (1997), Scatterometer data interpretation: Estimation and validation of the transfer function CMOD4, *J. Geophys. Res.*, **102**, 5767-5780.
5. Monaldo F., Kerbaol V., & the SAR Wind Team (2003), The SAR measurement of ocean surface winds: An overview, *Proc. 2nd Workshop on Coastal and Marine Applications of SAR*, 8-12 September 2003, Svalbard, Norway.
6. Li, X., Dong, Ch., Clemente-Colon, P., Pichel, W.G., & Friedman, K.S. (2004), Synthetic aperture radar observation of the sea surface imprints of upstream atmospheric solitons generated by flow impeded by an island, *J. Geophys. Res.* **109**, C02016, doi:10.1029/2003JC002168.
7. Chan, P.W., Cheng, C.M., & Alpers, W. (2010), Study of wind fields associated with subtropical squall lines using ENVISAT synthetic aperture radar images and ground-based weather radar data. *Int. J. Remote Sensing*, in press.
8. Melsheimer, C., Alpers, W., & Gade, M. (1998), Investigation of multi-frequency/multi-polarization radar signatures of rain cells over the ocean using SIR-C/X-SAR data, *J. Geophys. Res.*, **103**, 18867–18884.
9. Melsheimer, C., Alpers, W., & Gade, M. (2001), Simultaneous observations of rain cells over the ocean by the synthetic aperture radar onboard the ERS satellites and by surface-based weather radars, *J. Geophys. Res.*, **106**, 4665–4678.
10. Curry, J.M. & Murty, R.C. (1974), Thunderstorm-generated gravity waves, *J. Atmos. Sci.* **31**, 1402-1408.
11. Erickson, C.O. & Whitney, L.F. (1973), Picture of the month: Gravity waves following severe thunderstorms, *Mon. Wea. Rev.* **101**, 708-711.
12. Wong, W. K. (2010), Development of an operational rapid update non-hydrostatic NWP and data assimilation systems in the Hong Kong Observatory, *Preprint*, Hong Kong Observatory.

